POLITECNICO
MILANO 1863

SCUOLA DI INGEGNERIA INDUSTRIALE
E DELL'INFORMAZIONE

Beat Finder

Authors: ROBERTO GASTOLDI, CAMILLA MACCHINI, LUCA TRAMACERE

Academic year: 2024-2025

1. Introduction

Cardiac arrhythmia refers to abnormal heart rhythms caused by a variety of factors, including structural abnormalities and more complex underlying diseases. This phenomenon is highly variable and challenging to study, especially through non-invasive methods. The standard clinical tool used for diagnosis is the electrocardiogram (ECG). However, ECGs provide only an indirect view of the underlying electrical activity, which occurs on a much smaller spatial scale (typically within a few millimeters) making accurate localization difficult.
Specific arrhythmias such as ventricular tachycardia and atrial fibrillation are often initially treated with medication. Nevertheless, as the disease progresses and symptoms worsen, pharmacological treatment becomes less effective. At this stage, interventional procedures targeting the pathological tissue regions become the preferred therapeutic approach. A major challenge in these interventions lies in the lack of consensus on the precise location of the pathological area responsible for the arrhythmia.
The aim of this project is to develop an algorithm capable of identifying these critical regions using data acquired from electroanatomical maps. During the procedure, a catheter is inserted through the femoral vein and guided through the heart chambers. The catheter, while it's open, features a star-shaped structure with 20 sensors (four per arm), each of which records both the electrical signal and the corresponding two-dimensional position on the endocardial surface.

2. Checkpoint 1

Problem Description

The first checkpoint requires the development of an algorithm to identify focal activity from the traces of the given 20 unipolar signals.
The algorithm must return the following outputs:
1. **Activation Annotations**: for each of the 20 signals, generate a list of activation times. These activation times correspond to the local minima of the first derivative of the signal, indicating the moments of depolarization at each electrode.
2. **Morphology Classification**: assign a local morphology score $LS \in \{0, 0.5, 1\}$ to each detected activation, based on the waveform shape:
    - $LS = 0$: *QS morphology* — Characterized by a single negative deflection (monophasic wave).
    - $LS = 0.5$: *Intermediate QS-RS morphology* — Represents a transition between QS and RS morphologies and indicates potential proximity to a focal activity.
    - $LS = 1$: *RS complex* — Defined by a positive R-wave followed by a negative S-wave (biphasic morphology).

The layout of the sensors is illustrated in Figure 1, while Figure 2 provides an example of the recorded signals.
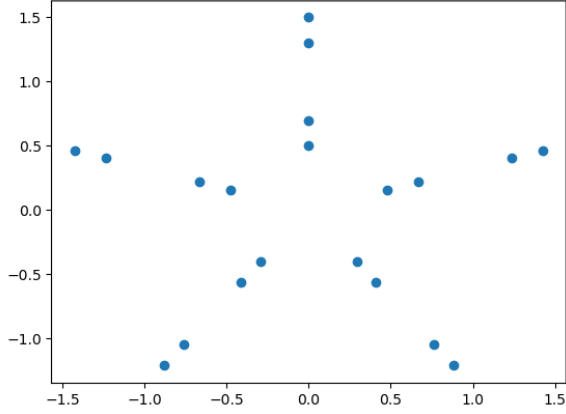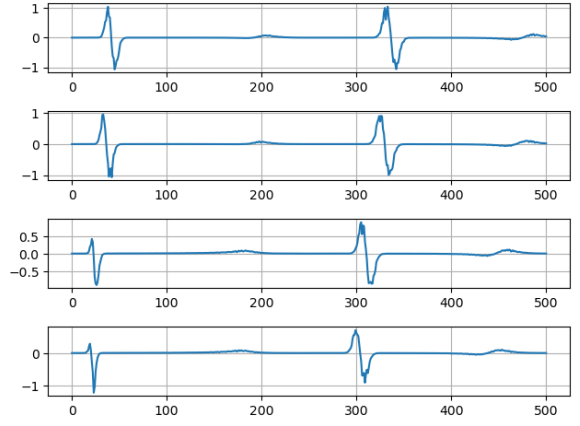
Figure 1: Plot of the sensors' positions

Figure 2: Example of the four unipolar signals measured by an arm of the catheter.

Mathematical Formulation

Let $S_i(t): [0, T] \to R$ denote the unipolar electrogram recorded from the i-th electrode, with $i = 1, \dots, 20$, and t denoting time. Each signal contains one or more depolarization events, manifesting as sharp deflections in the waveform.

1. Activation Time Detection. We define the activation times $T_{i,k} \in [0, T]$ for electrode i, where $k = 1, \dots, K_i$, as local minima of the time derivative $D_i(t) := \frac{dS_i(t)}{dt}$. Formally, $T_{i,k}$ satisfies:

$$T_{i,k} \in \arg\min_{t \in \mathcal{N}_k} D_i(t),$$

where $\mathcal{N}_k = [t_k - \delta, t_k + \delta]$ is a small temporal neighborhood centered around candidate event windows t_k, obtained via heuristic thresholding or signal energy criteria.

We assume the signal is sufficiently smooth: $S_i(t) \in C^1([0, T])$, so $D_i(t)$ exists and is continuous.

2. Morphology Classification. Given an activation time $T_{i,k}$, we define a signal window $\mathcal{W}_{i,k} = [T_{i,k} - \tau, T_{i,k} + \tau]$, over which the waveform morphology is assessed.

We define the local morphology score $LS_{i,k} \in \{0, 0.5, 1\}$ using the following logic:

$$LS_{i,k} = \begin{cases} 1, & \text{if } \exists\, t_r < t_s \in \mathcal{W}_{i,k} \text{ s.t. } S_i(t_r) > 0,\ S_i(t_s) < 0 \quad \text{(RS complex)} \\ 0, & \text{if } S_i(t) < 0\ \forall t \in \mathcal{W}_{i,k} \quad \text{(QS morphology)} \\ 0.5, & \text{otherwise} \quad \text{(intermediate morphology).} \end{cases}$$

In practice, we apply a band-pass filter to $S_i(t)$, normalize amplitude, and discretize time into steps $t_j = j\Delta t$, evaluating finite-difference approximations to detect $T_{i,k}$, and perform morphology analysis over a fixed-length window centered at each detection.

3. Output. The final output of the algorithm is a set:

$$\mathcal{A}_i = \{(T_{i,k}, LS_{i,k})\}_{k=1}^{K_i}, \quad i = 1, \dots, 20.$$

Each element represents a detected depolarization event and its associated local waveform morphology.

Proposed algorithms

Addressing the first challenge is relatively straightforward, but it requires careful consideration of one key aspect: as shown in Figure 2, the measurements are affected by noise, which can significantly impact the detection of activation points.

To mitigate this issue, each of the 20 signals is first normalized and then processed using a low-pass filter. This preprocessing step helps reduce the influence of noise, ensuring more accurate detection of local minima.

Once the signals are filtered, the time derivative is computed, and activation times are identified as the points where the derivative reaches a local minimum.

A summary of the entire procedure is outlined in Algorithm 1.

Algorithm 1 Activation Annotation

    Input: Signals $S_i(t)$, $i = 1, 2, \ldots, 20$

    Normalize all 20 Signals and apply a low-pass filter to each.

    for $i = 1, 2, \ldots, 20$ **do**

        Compute $D_i(t)$

        Detect the *activation times* $T_{i,1}$ and $T_{i,2}$

    end for

The second task is slightly more challenging and requires a more nuanced approach. For each signal, a window of 100 samples centered around each activation time is extracted (i.e., 50 samples before and 50 after the activation). This ensures that the entire depolarization waveform is captured.

Next, the algorithm analyzes the signal within this window by detecting both positive and negative peaks. The morphology is then classified based on the ratio between the maximum positive and maximum negative peak amplitudes. Depending on this ratio and a predefined threshold, the morphology is classified as either RS (score = 1), QS (score = 0), or intermediate QS-RS (score = 0.5).

For the intermediate class, a confidence score is assigned based on how close the peak ratio is to the classification threshold. The closer the ratio is to the threshold, the lower the confidence in the classification. At this stage. After the initial morphology classification, scores assigned as 0.5 (intermediate QS-RS) are further refined using both the confidence score and the timing of the activation. The goal is to resolve ambiguous cases where the waveform does not clearly fall into a QS or RS category.

This refinement is based on the deviation of each activation time from the global mean across all sensors, normalized by the standard deviation. If an activation occurs significantly earlier than the average and has high classification confidence, it is likely to be a true QS morphology (score = 0). Conversely, if the activation is late and the confidence is low, it is more likely to represent an RS morphology (score = 1).

The adjusted classification helps in improving the spatial coherence of the detected morphologies and increases the robustness of focal source identification.

A summary of the procedure is outlined in Algorithm 2.

Algorithm 2 Morphology Classification

    Input: Windowed signal segment of length 100

    Parameters: `threshold`=0.05, `thresh_ratio`=0.5

    Detect positive peaks with prominence $> $ `threshold` $\cdot \max(|\text{signal}|)$

    Detect negative peaks in the same way (by inverting the signal)

    if only negative peaks are found **then**

        return Morphology score = 0, confidence = 1

    else if only positive peaks are found **then**

        return Morphology score = 1, confidence = 1

    else if both positive and negative peaks are found **then**

        Compute peak ratio: $r = \max(\text{positive})/|\max(\text{negative})|$

        if $r > $ `thresh_ratio` **then**

            return Morphology score = 1, confidence = 1

        else

            Set confidence: $1 - r/$`thresh_ratio`

            return Morphology score = 0.5, confidence

        end if

    end if

    Refine intermediate scores (0.5) using confidence
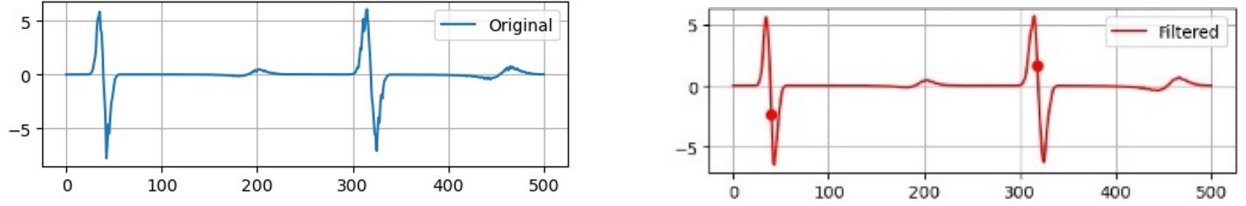

Numerical results

Figure 3: Example of a recorded signal from a single sensor. On the left the original signal is shown while on the right we have the filtered one and the detected activation times.
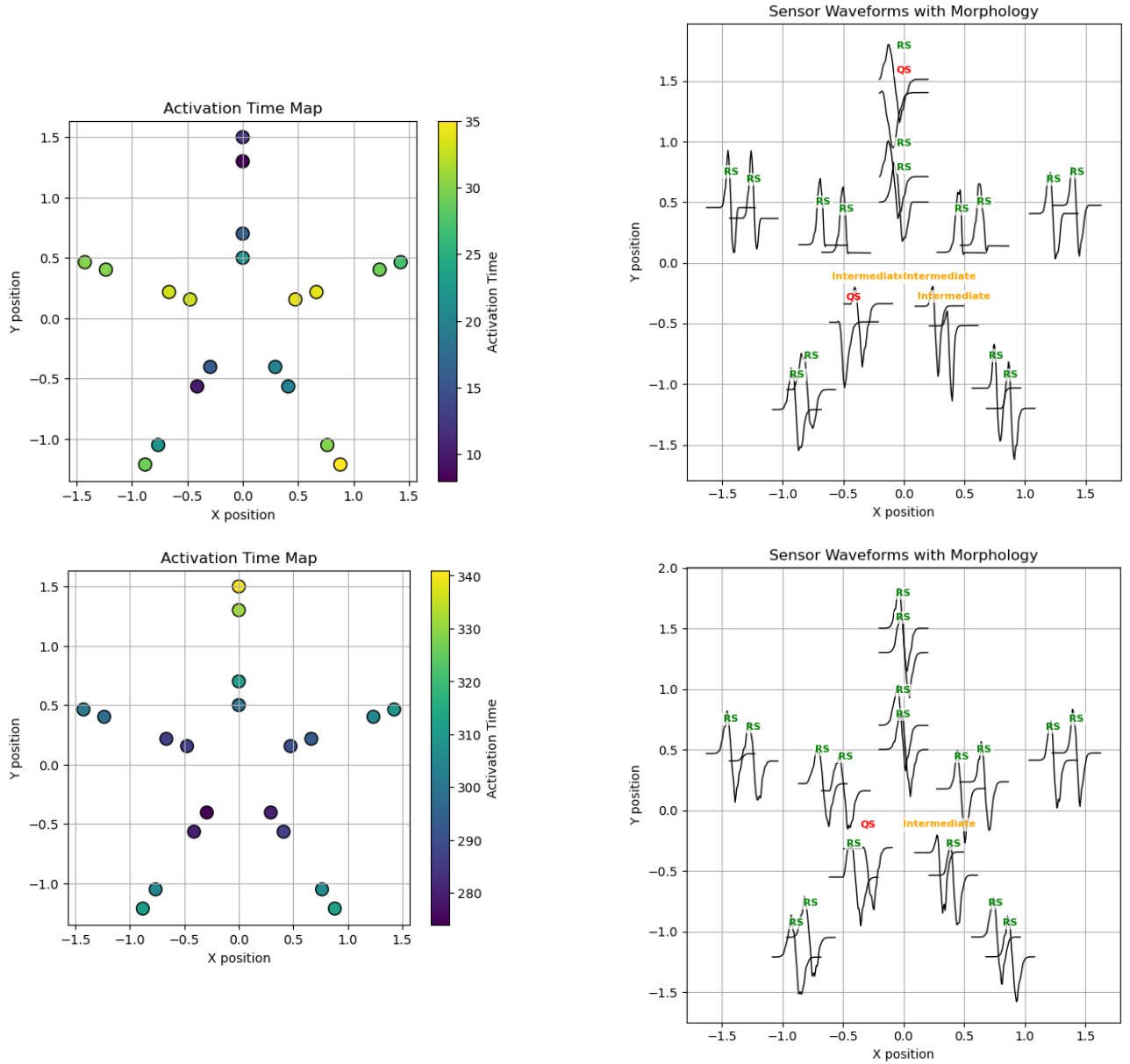

Figure 4: Results for the patient number 13.

The results obtained are quite promising. As shown in Figure 3, the activation times detected on the filtered signals appear consistent and well-localized. This highlights the importance of the preliminary preprocessing operations: without proper filtering, the signals would likely have led to ambiguous interpretations, such as the

detection of activation times before the first positive peak or after the negative peak, which would compromise the reliability of the analysis.

Figure 4 shows the output of the proposed algorithm for one specific patient in the dataset (patient number 13). On the left, the activation times measured at each sensor are plotted, while on the right, the corresponding impulse morphologies are classified.

This second plot allows for further comments. The morphology classification algorithm relies on relatively simple and local rules, based on the ratio between the peaks of each signal. Once a signal is classified as RS with high confidence, it is no longer updated or refined, even if it lies in the vicinity of a QS morphology. This behavior is evident in the upper-right part of Figure 4, where a QS morphology is correctly detected in the second (vertical) catheter arm, but no surrounding signals are labeled as intermediate. This is suboptimal, as one would expect a gradual morphological transition when approaching a QS, reflected by the presence of intermediate morphologies.

A potential improvement to the algorithm could involve incorporating spatial correlations among adjacent sensors. However, such an enhancement would increase the computational cost, which may negatively impact the algorithm's efficiency—currently one of its strongest aspects, alongside accuracy.

3.   Checkpoint 2

The second checkpoint focuses on developing an algorithm to localize focal activity sites within cardiac tissue, based on a set of unipolar electrograms. Each scenario in the dataset contains signals from 20 electrodes and exhibits two separate wavefront activations. The task is to estimate the coordinates of four distinct impulse sites: two associated with the first activation wavefront, and two with the second.

Problem Description

This task constitutes a classical inverse problem in cardiac electrophysiology: infer the origin of excitation wavefronts from observed activation patterns. In contrast to a forward simulation, where known physical parameters are used to generate activation maps, the inverse setting requires estimating unknown parameters that best explain the given data.

We are provided with a set of activation times $\{T_i\}_{i=1}^N$ at spatial sensor locations $\{(x_i, y_i)\}_{i=1}^N \subset \Omega \subset R^2$, where $N = 20$. Each dataset scenario contains two temporally separated wavefronts. These wavefronts are assumed to originate from unknown focal points in the domain, denoted as $\{(x_j^{(k)}, y_j^{(k)})\}_{j=1}^2$ for wavefront $k = 1, 2$.

Mathematical Formulation

Forward model.   Activation times $T(x, y)$ over the tissue domain $\Omega = [-2, 2]^2$ are modeled by the anisotropic Eikonal equation:

$$c_v \sqrt{\nabla T(x,y)^T D(x,y) \nabla T(x,y)} = 1, \quad (x,y) \in \Omega, \tag{1}$$

subject to initial conditions at the focal sites:

$$T(x_j^{(k)}, y_j^{(k)}) = 0, \quad \text{for } j = 1, 2 \text{ and } k = 1, 2.$$

Here, $c_v > 0$ is the global conduction velocity, and $D(x, y) \in R^{2 \times 2}$ is the local diffusion tensor capturing tissue anisotropy, given by:

$$D(x,y) = \vec{b}(x,y) \otimes \vec{b}(x,y) + \frac{1}{a_{\text{ratio}}} \vec{a}(x,y) \otimes \vec{a}(x,y), \tag{2}$$

where $\vec{b}(x, y)$ is the normalized fiber direction and $\vec{a}(x, y)$ is its orthogonal counterpart. The anisotropy ratio $a_{\text{ratio}} \geq 1$ reflects slower conduction across fibers.

Inverse problem.   Let $\mathbf{p} := \left\{ (x_j^{(k)}, y_j^{(k)})_{j=1}^2 \right\}_{k=1}^2$ denote the set of all impulse site locations to be estimated. Given measured activation times $\{T_i^{\text{obs}}\}_{i=1}^N$ at known sensor locations $\{(x_i, y_i)\}$, the inverse problem can be cast as a PDE-constrained optimization problem:

$$\min_{\mathbf{p}} \ \mathcal{J}(\mathbf{p}) := \frac{1}{2} \sum_{i=1}^N \left(T(x_i, y_i; \mathbf{p}) - T_i^{\text{obs}} \right)^2, \tag{3}$$

subject to:

$$c_v \sqrt{\nabla T(x,y)^T D(x,y) \nabla T(x,y)} = 1, \quad T(\mathbf{p}) = 0. \tag{4}$$

Assumptions.   We assume:
- c_v and a_{ratio} are known and fixed (calibrated from prior data or simulations).
- Fiber field $\vec{b}(x, y)$ is smooth and known a priori.
- Each wavefront originates from exactly two point sources.

Proposed algorithms

Parameter estimation.   The first task of this checkpoint involves estimating the electrophysiological tissue parameters, which we assume to be shared across all future patients. To achieve this, we estimate the optimal (c_v, a_{ratio}) pairs for each impulse in the dataset by minimizing the discrepancy between simulated and measured activation times.

The estimation is performed using the Powell optimization method. The loss function used is:

$$\mathcal{L}(\mu) = \sum_{i=1}^{20} \left(T_{\text{obs}}^{(i)} - T_{\text{model}}(x_i, y_i; \mu) \right)^2$$

where the parameter vector $\mu = (a_{\text{ratio}}, c_v, t_0, t_1)$ includes the anisotropy ratio, conduction velocity, and the initial activation times of the two focal sites. T_{obs} is computed using the activation time detection algorithm developed in Checkpoint 1, while T_{model} is obtained from the anisotropic fast marching method (FMM) described in [1], which was already implemented.

To ensure robustness, for each impulse the optimization is carried out over multiple random initializations. The parameters are sampled within the following ranges:
- $a_{\text{ratio}} \in [8.0, 9.5]$
- $c_v \in [65, 85]$
- $t_0, t_1 \in [0, 5 \times 10^{-2}]$

Once a set of (c_v, a_{ratio}) values has been estimated for each impulse in the dataset, we compute their sample mean. This global average is then used in the second task—localizing the impulse sites—under the assumption that these properties remain constant across patients.

Focal impulse site location   While optimization-based methods provide interpretability and rely on solid theoretical foundations, they often require computationally intensive iterative solvers, limiting their suitability for real-time applications. As an alternative, we adopt a data-driven approach based on convolutional neural networks (CNNs) to directly reconstruct the activation time field and infer the focal impulse locations.

Once trained, the CNN enables rapid inference, several orders of magnitude faster than traditional solvers, while retaining sufficient accuracy for practical use. In this work, we demonstrate the network's ability to identify the origin of two propagating wavefronts using only 20 unipolar electrogram measurements, effectively bypassing the numerical solution of the Eikonal equation. This architecture enables fast and generalizable predictions across varying tissue geometries and conduction properties.

Synthetic dataset generation   To train and evaluate the model, we generate a dataset of synthetic activation patterns simulating dual focal sources in an anisotropic medium. Each sample consists of a 64×64 activation map, computed analytically using an anisotropic propagation model with two foci randomly located within a 3×3 cm region. The sources activate at controlled time offsets, and propagation speed varies with orientation according to a fixed anisotropy ratio.

Electrogram signals are sampled at 20 fixed sensor positions, with up to two positions randomly occluded to simulate real-world sensor dropout. In total, the dataset includes 10,000 input–target pairs, where the input is a sparse activation map and the target is the full field.

Input representation   Each CNN input is a $64 \times 64 \times 1$ tensor representing the spatial distribution of activation times, where valid measurements are assigned to 20 sensor positions and all other pixels are masked with a constant value of -1.0 to denote missing data.

The activation maps are defined over a $[-2, 2] \times [-2, 2]$ cm domain, with sensors placed at fixed radial distances and angles to mimic realistic catheter configurations. In 40% of the samples, two sensors are randomly excluded to increase robustness to occlusion. The ground truth is the complete activation time field, also with shape $(64, 64, 1)$, used as the network's regression target.
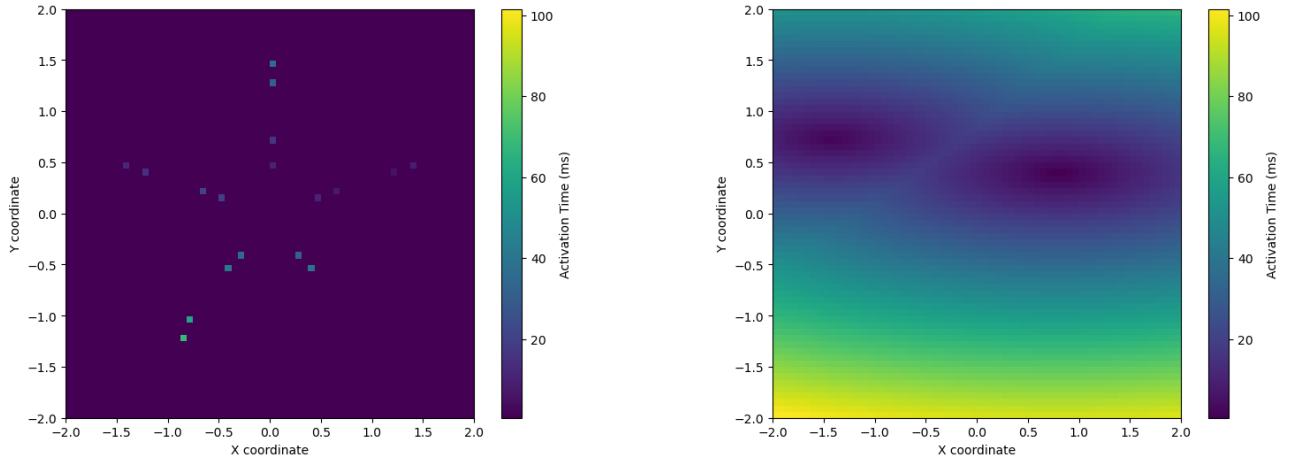
Figure 5: (Left) Example input: masked activation map with values at 18 sensor locations. (Right) Expected output: full activation time field reconstructed by the CNN.

Architecture   The reconstruction model adopts a convolutional autoencoder architecture composed of an encoder and a decoder with skip connections, inspired by U-Net-like designs.

Encoder: Extracts multi-scale features from the input masked activation maps using convolutional layers with residual connections and downsampling to create a compact latent representation.

Decoder: Reconstructs the full activation field by progressively upsampling the latent features, leveraging skip connections from the encoder for detailed spatial information. Regularization via dropout and residual blocks is applied for stable training.

Residual blocks: Both encoder and decoder use residual convolutional units with batch normalization and nonlinear activations to facilitate gradient flow and improve learning.
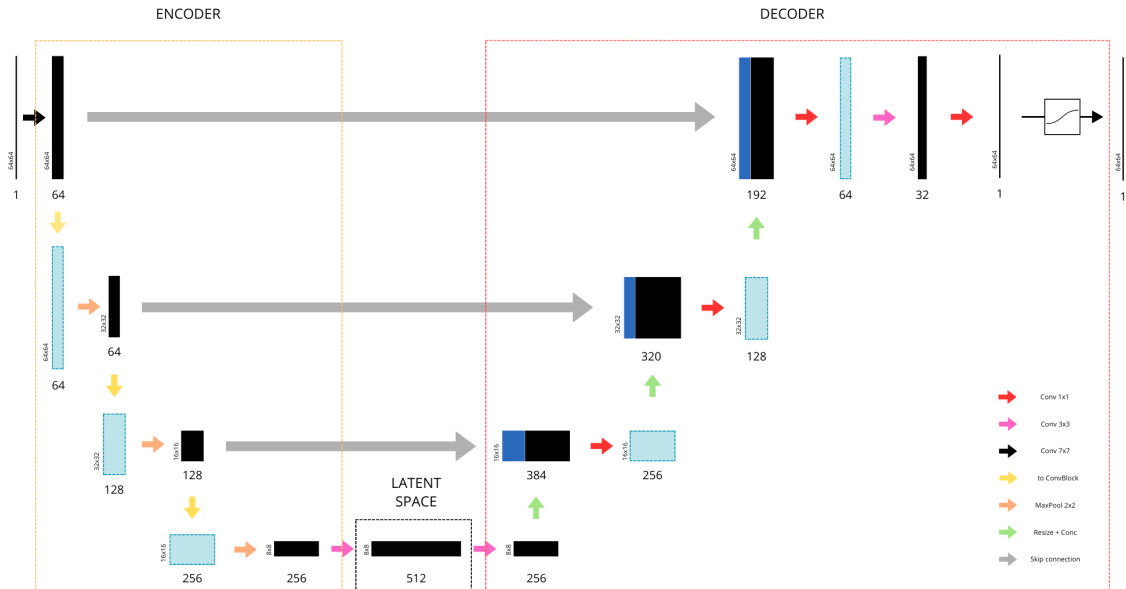

Figure 6: Schematic diagram of the CNN autoencoder architecture used for reconstructing activation time fields.

Training setup The model is trained on 65% of the dataset, with 35% used for validation. We optimize the loss using Adam with an initial learning rate of 10^{-4}, applying exponential decay over training. A custom loss function combines mean absolute error, structural similarity index (SSIM), and a masked MSE at known electrode locations.

Training runs for up to 100 epochs with early stopping based on validation loss. No data augmentation is applied, as the electrode layout is fixed. Model checkpoints and visualizations are saved throughout training.

Focal Site Identification After reconstructing the pressure field, we extract the most probable focal locations through a two-step process: detection of local minima and their refinement to subpixel accuracy.

The detection stage evaluates a central region of the field, excluding borders, and identifies candidate locations whose values are:

- strictly the minimum in their 3×3 neighborhood, and
- below a global threshold (scaled relative to the field's dynamic range).

To achieve this efficiently, we vectorize the test across grid coordinates using `vmap`, and return a fixed-size array of candidate minima.

Each detected minimum is then refined using second-order interpolation. The method estimates first and second-order derivatives via finite differences and applies a Newton-like update to adjust the position:

$$x^* = x - \frac{\partial_x f}{\partial_{xx} f + \varepsilon}, \qquad y^* = y - \frac{\partial_y f}{\partial_{yy} f + \varepsilon}$$

with ε a small constant to avoid division by zero. The resulting positions are finally normalized to match the domain of the network output.

If fewer than the desired number of minima are found, the output is padded to maintain shape consistency.

Numerical results

Parameter estimation The results of the estimated anysotropic ratio and conduction velocity are $(8.7, 74.22)$, all the estimates are shown in Table 2.

	$a_{\mathbf{ratio}}$	c_v	t_0	t_1	**MSE**
Scenario 1	8.37853493	79.3153527	$1.80649733 \times 10^{-3}$	$3.22900958 \times 10^{-3}$	1.20
	8.85162095	69.9358734	$2.17176371 \times 10^{-3}$	$8.98866123 \times 10^{-6}$	2.06
Scenario 2	8.54322246	79.2568385	$2.85153154 \times 10^{-4}$	$7.80147242 \times 10^{-4}$	1.27
	9.04496459	68.2075520	$1.82205105 \times 10^{-3}$	$4.77661598 \times 10^{-5}$	2.73
Scenario 3	9.17460168	74.6050706	$2.22698366 \times 10^{-3}$	$2.10901577 \times 10^{-3}$	1.73
	8.50494359	69.8065402	$5.66330090 \times 10^{-3}$	$1.79527831 \times 10^{-4}$	2.25

Table 1: Parameters estimation

These values are computed as a weighted average of all estimates, using weights inversely proportional to their corresponding MSEs.

The weighted mean $\hat{\boldsymbol{\mu}}$ of the estimated parameters is computed as:

$$\hat{\boldsymbol{\mu}} = \sum_{i=1}^{6} w_i \boldsymbol{\mu}_i, \quad \text{where} \quad w_i = \frac{1/\mathrm{MSE}_i}{\sum_{j=1}^{n} 1/\mathrm{MSE}_j}, \quad \boldsymbol{\mu}_i = (a_{\mathrm{ratio},i}, c_{v,i})$$

Here, $\boldsymbol{\mu}_i$ denotes the i-th estimated vector of parameters, and w_i are weights inversely proportional to their associated mean squared error MSE_i.

Focal impulse site location We evaluate the trained neural network on a held-out test set composed of 500 synthetic samples, each simulating two focal activation wavefronts. The network successfully reconstructs the activation time field and infers the underlying impulse source locations using only 20 sparse electrogram measurements per sample.

Figure 7 shows the training and validation loss curves alongside the learning rate schedule, demonstrating stable convergence and generalization. Representative reconstruction results are shown in Figure 8, including the input measurements, predicted field, ground truth, and corresponding error maps.

To quantitatively assess model performance, we compute error metrics over the entire test set. Specifically, we report the mean absolute error (MAE), root mean squared error (RMSE), 95th percentile error, and maximum error between the predicted and true activation fields. All metrics are reported in milliseconds (ms).

The results, summarized in Table 2, show that the network achieves a mean absolute error of 1.23 ms and a 95th percentile error of 4.00 ms across the full domain, with a worst-case error of 58.04 ms. These values confirm that the network provides accurate reconstructions even under sparsely sampled and occluded measurement conditions.

Metric	MAE (ms)	RMSE (ms)	95th Perc (ms)	Max Error (ms)
Activation Field Error	1.23	2.47	4.00	58.04

Table 2: Error metrics computed on the reconstructed activation field across 500 test samples. All values are reported in milliseconds.
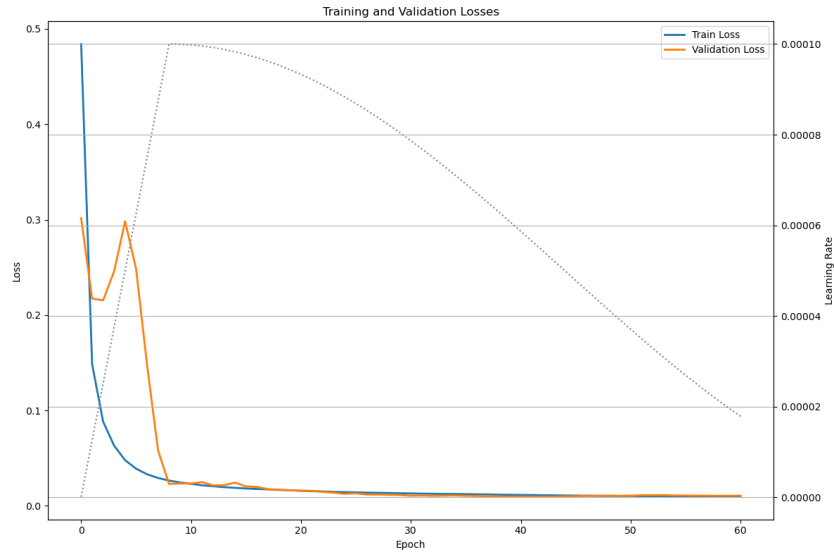
Figure 7: Training and validation loss curves with learning rate schedule.
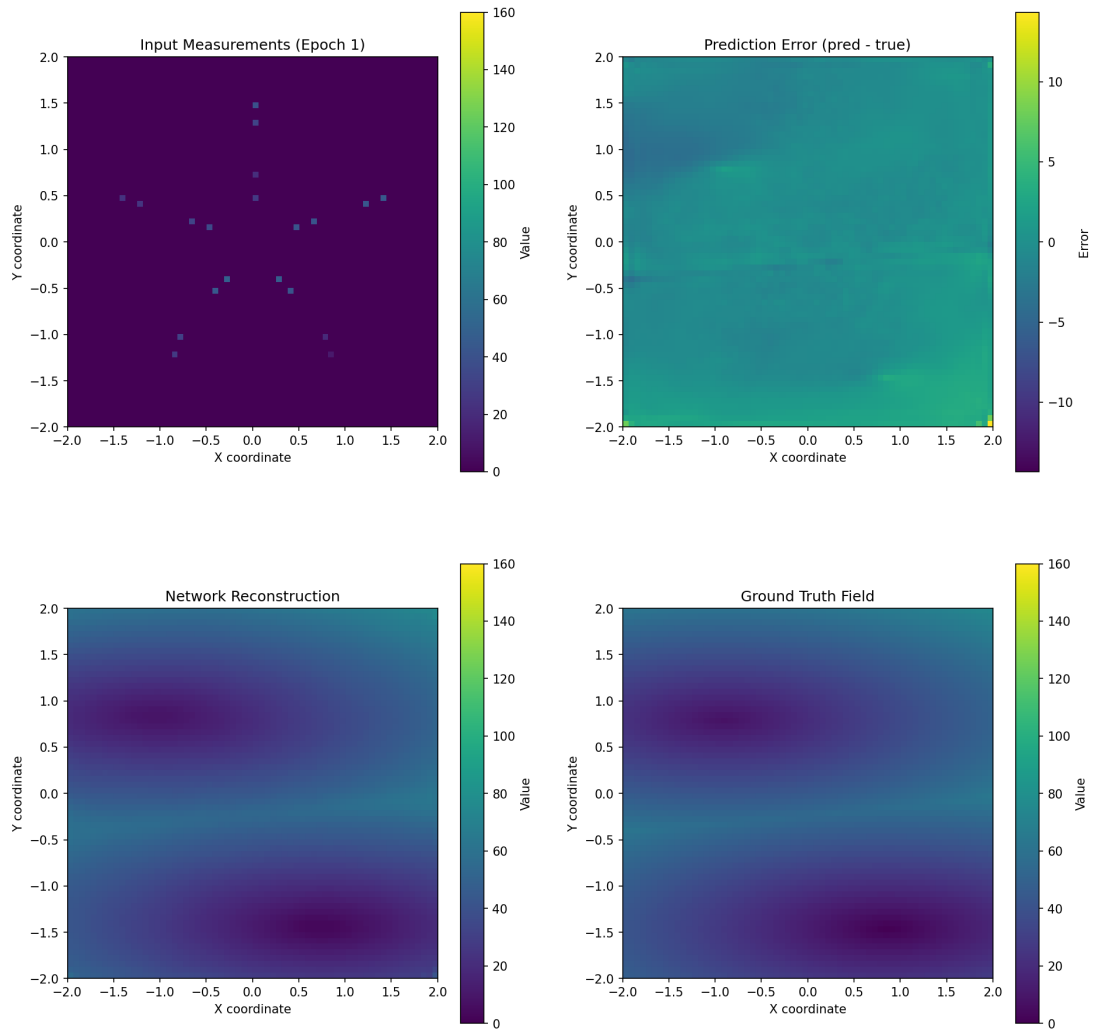

Figure 8: Examples of reconstructed activation fields. Each field shows: (i) input image, (ii) prediction error, (iii) predicted activation field, and (iv) ground truth.

4.   Checkpoint 3

Problem Descriprion

The third checkpoint requires the development of an algorithm to reconstruct activation times of a pair of malfunctioning sensor from the traces of remaining 18 unipolar signals. Also in this case, a dataset with 3 patients and their unipolar signals were provided.

Mathematical Formulation

Let $\Omega \subset R^2$ denote the spatial domain containing $N = 20$ sensors located at positions $\{(x_i, y_i)\}_{i=1}^{20} \subset \Omega$. Each sensor records a 1D time series $S_i(t)$, from which we extract an activation time $T_i = T(x_i, y_i)$ representing the earliest time of arrival.
Let $\mathcal{B} \subset \{1, \ldots, N\}$ be the index set of broken sensors, with $|\mathcal{B}| = 2$. The goal is to estimate the activation times T_i for $i \in \mathcal{B}$, relying only on the uncorrupted times $\{T_j\}_{j \notin \mathcal{B}}$.

Forward Model.   We assume that activation originates from a point source at $\mathbf{x}_s = (x_s, y_s)$ and propagates anisotropically through the medium. The arrival time field $T(x)$ satisfies the anisotropic Eikonal equation:

$$\|\nabla T(x)\|_D = 1, \qquad x \in \Omega, \quad T(\mathbf{x}_s) = 0, \tag{5}$$

where $D \in R^{2 \times 2}$ is a symmetric positive-definite matrix that defines the anisotropic propagation metric. The induced norm is defined as $\|v\|_D^2 := v^\top D v$.
In this setting, the analytical solution for $T(x)$ is:

$$T(x) = \sqrt{(x - \mathbf{x}_s)^\top D(x - \mathbf{x}_s)}. \tag{6}$$

Inverse Problem.   Given observed activation times $\{T_j^{\text{obs}}\}_{j \notin \mathcal{B}}$, we aim to infer:
- The source location $\mathbf{x}_s \in \Omega$
- The anisotropy matrix $D = D^\top \succ 0$
- The activation times $\{T_i\}_{i \in \mathcal{B}}$ for the broken sensors

This leads to the nonlinear least-squares problem:

$$\min_{\mathbf{x}_s \in \Omega, D = D^\top \succ 0} \mathcal{J}(\mathbf{x}_s, D) = \sum_{j \notin \mathcal{B}} w_j \left(T_j^{\text{obs}} - \sqrt{(x_j - \mathbf{x}_s)^\top D(x_j - \mathbf{x}_s)} \right)^2, \tag{7}$$

with $w_j = 1$ for $j \notin \mathcal{B}$ and $w_j = 0$ otherwise.

Proposed algorithms

Time Estimation.   This algorithm combines neural network predictions with physics-informed optimization. Each patient provides 20 unipolar electrograms $S_i(t)$, from which we first extract the activation times using the Checkpoint 1 algorithm. Malfunctioning sensors, defined as those with zero first activation time, are removed from the data.
The remaining signals are used to estimate candidate focal impulse site positions using convolutional neural network developed for Checkpoint 2, which was also trained to handle input with 18 working sensors out of 20. The estimated coordinates are then leveraged to guide a subsequent optimization step.
The core of the reconstruction procedure is a Differential Evolution (DE) optimizer that minimizes a physics-based loss function. Specifically, the forward model computes expected activation times at each sensor based on a parameterized wave propagation velocity field and focal impulse site parameters. The DE search is initialized using the focal site coordinates and activation times predicted by the neural network, which are also used to define tighter spatial and temporal bounds for the optimization variables.
To prevent the optimization from being biased by the corrupted entries, a binary weight mask is applied that zeroes out the residuals corresponding to the malfunctioning sensors during the loss computation. After the optimization converges, the reconstructed activation times at the broken sensor positions are computed using the fitted parameters and the physical propagation model. A summary of the full procedure is presented in Algorithm 3.

Algorithm 3 Broken Sensor Time Estimation

Input: Signals $S_i(t)$, $i = 1, 2, \ldots, 20$
Step 1:
    Extract activation times using Algorithm 1
    Identify malfunctioning sensors (first activation time = 0)
    Remove corresponding signals from the observation set
Step 2:
    Estimate focal impulse site coordinates using Checkpoint 2
Step 3:
    Apply Differential Evolution to find the true impulse sites coordinates
    Use optimized parameters to reconstruct activation times at broken sensor positions
Output: Estimated activation times at malfunctioning sensors

Uncertainty Quantification. It is important to highlight that estimating the activation times at the malfunctioning sensor locations involves multiple steps, each introducing a source of uncertainty. These include the activation time extraction, the estimation of the focal impulse site locations, and finally the signal reconstruction via the Eikonal equation. The latter depends on two parameters, c_v and a_{ratio}, which were estimated in Checkpoint 2 and assumed to be universally valid across all patients.

Accounting for all sources of uncertainty is a complex task. However, in order to provide a possible confidence interval for the final estimates, we adopt a Monte Carlo-based approach. Using the parameter estimates collected in Table 2, we computed the weighted mean and weighted covariance matrix:

$$\hat{\boldsymbol{\mu}} = \begin{bmatrix} 8.7 \\ 74.22 \end{bmatrix}, \quad \hat{\boldsymbol{\Sigma}} = \begin{bmatrix} 0.1037 & -0.7799 \\ -0.7799 & 24.5065 \end{bmatrix}$$

Assumption: $\mathbf{X} = (c_v, a_{\text{ratio}}) \sim \mathcal{N}_2(\hat{\boldsymbol{\mu}}, \hat{\boldsymbol{\Sigma}})$
QoI: $T = (T_{1,k}(\mathbf{X}), \ T_{2,k}(\mathbf{X}))$

Algorithm 4 Uncertainty Quantification

After **Step** 2 of Algorithm 3:
Sample $(c_v^{(1)}, a_{\text{ratio}}^{(1)}), \ldots, (c_v^{(N)}, a_{\text{ratio}}^{(N)}) \sim \mathcal{N}_2(\hat{\boldsymbol{\mu}}, \hat{\Sigma})$
for $i = 1$ **to** N **do**
    Estimate $T_{1,k}^{(i)}$ and $T_{2,k}^{(i)}$ using Algorithm 3 with parameters $(c_v^{(i)}, a_{\text{ratio}}^{(i)})$, for $k = 1, 2$
end for
Compute sample means $\bar{T}_{1,k}, \bar{T}_{2,k}$ and standard deviations $\hat{\sigma}_{1,k}, \hat{\sigma}_{2,k}$, for $k = 1, 2$
return $\bar{T}_{1,k}, \bar{T}_{2,k}$ and their confidence intervals

---

Recall that the structure of the confidence interval is:

$$I_\alpha(T_{j,k}) = \left(\bar{T}_{j,k} - z_{1-\frac{\alpha}{2}} \cdot \frac{\hat{\sigma}_{j,k}}{\sqrt{N}}, \quad \bar{T}_{j,k} + z_{1-\frac{\alpha}{2}} \cdot \frac{\hat{\sigma}_{j,k}}{\sqrt{N}} \right), \quad \text{for } j = 1, 2; \ k = 1, 2$$

,
where $z_{1-\frac{\alpha}{2}}$ is the $1 - \frac{\alpha}{2}$ quantile of a standard Gaussian distribution.

Numerical Results

For the Monte Carlo evaluation, we selected $N = 25$ samples. This value strikes a balance between computational efficiency and the precision of confidence intervals: larger N would reduce uncertainty, but the marginal benefit was not sufficient to justify the increased cost. The choice of $N = 25$ ensured reliable statistical estimates at a manageable computational cost.

The method demonstrated strong overall performance, achieving an average accuracy of **4.51 out of 5** across test cases. Figure 9 shows a representative example of the reconstruction process. The algorithm developed in Checkpoint 2 proved highly reliable for identifying the first impulse, even in the presence of missing sensors. While the reconstruction of the second impulse was more challenging, particularly due to the need to align signals with a 274 ms rescaling, the algorithm was still able to recover meaningful information in most cases.

These results confirm the robustness of the approach and its potential applicability in clinical or research settings involving focal source localization.
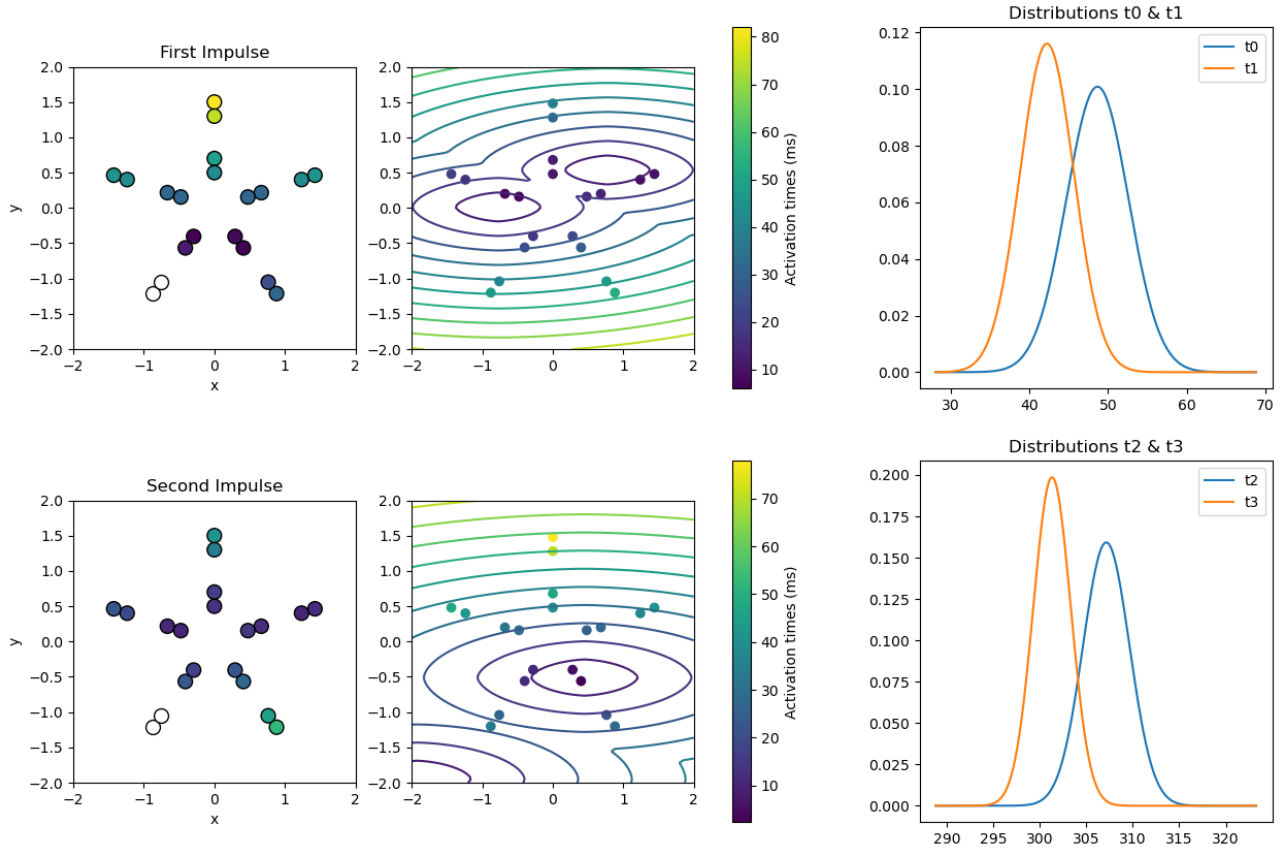

Figure 9: Example of `Checkpoint3` function on patient number 3.

5.   Conclusions

In this project, we addressed the problem of detecting arrhythmogenic sources from intracardiac recordings acquired via a star-shaped 20-electrode catheter. Our workflow included the development of algorithms to extract activation times and the design of both physics-based and data-driven methods for localizing focal impulses.

Among the different approaches explored, our final strategy, combining neural network-based initialization with anisotropic forward modeling and global optimization, proved particularly effective. The method achieved an accuracy of **4.51 out of 5**, demonstrating its reliability even under sensor dropout and signal distortions.

While certain aspects—such as precise recovery of multiple impulse sites—remain technically demanding, the core method is solid and has shown consistent, high-quality performance. The results indicate that our framework is not only functional but already mature enough to support further refinement or integration into practical workflows.

Appendix: Phisics Informed Neural Network (PINN)

Checkpoint 2 was initially addressed with the implementation of a Physics-Informed Neural Network. While the reconstructions are generally good, the absence of boundary conditions significantly limits accuracy in all areas of the domain.
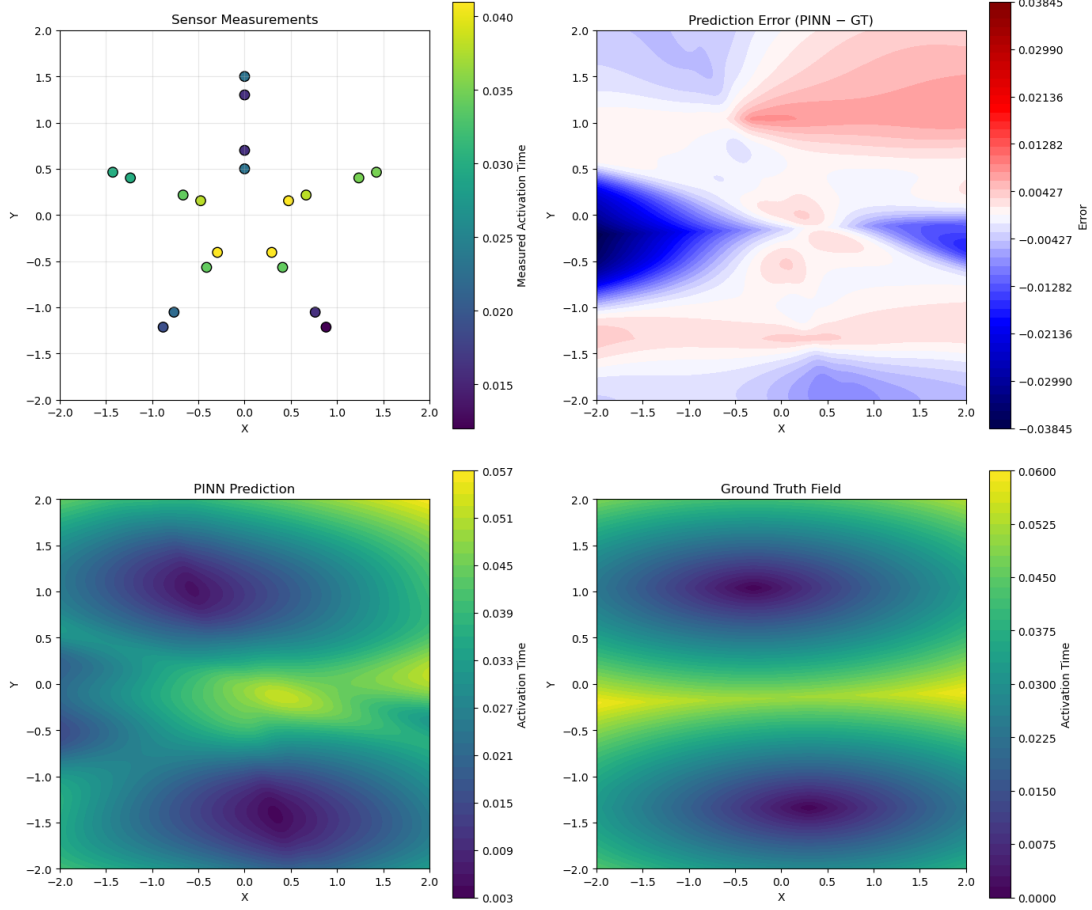

Figure 10: Examples of reconstructed activation fields. Each field shows: (i) input image, (ii) prediction error, (iii) predicted activation field, and (iv) ground truth.
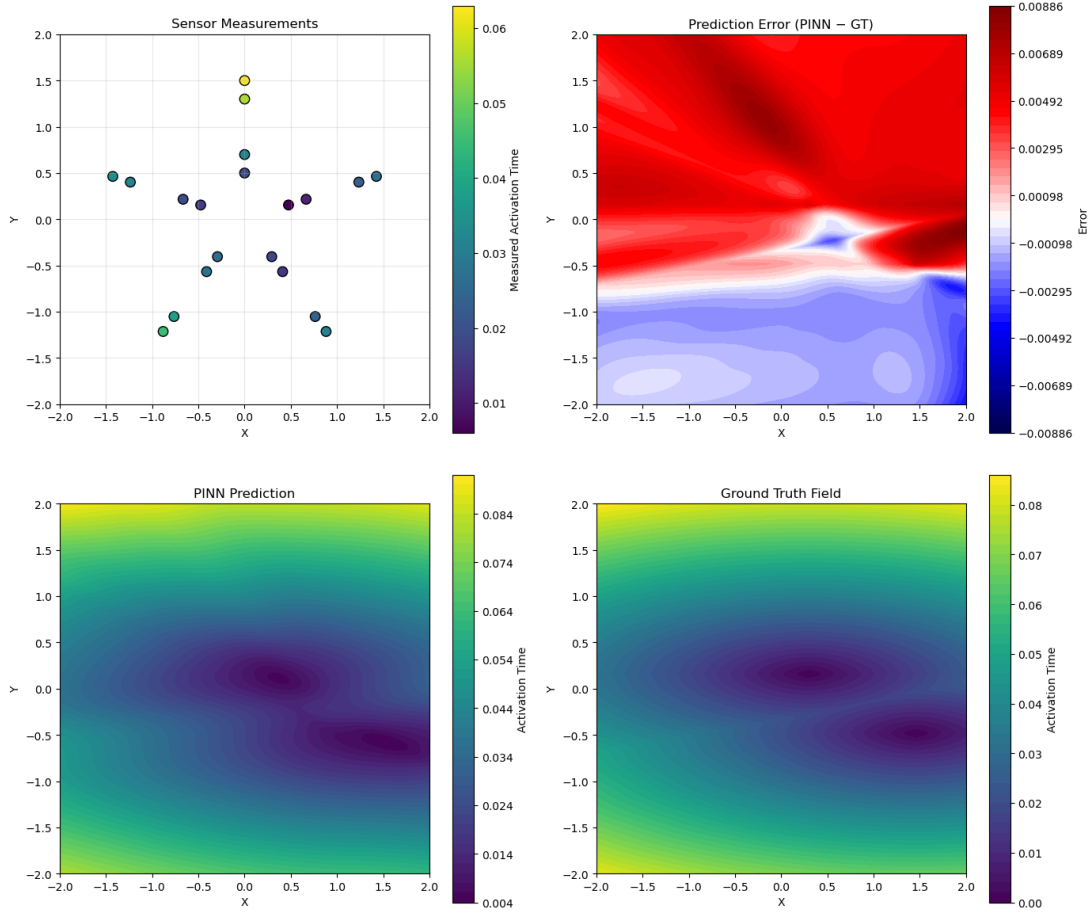
Figure 11: Examples of reconstructed activation fields. Each field shows: (i) input image, (ii) prediction error, (iii) predicted activation field, and (iv) ground truth.

References

[1] M. Sermesant, H. Delingette, and N. Ayache. An anisotropic multi-front fast marching method for real-time simulation of cardiac electrophysiology. In Heidelberg Springer, Berlin, editor, *Functional Imaging and Modeling of the Heart*, volume 4466, 2007.